AIAA JOURNAL
Vol. 44, No. 7, July 2006

Design of a Morphing Airfoil Using Aerodynamic Shape Optimization

M. Secanell* and A. Suleman†
University of Victoria, Victoria, British Columbia V8W 3P6, Canada
and
P. Gamboa‡
Universidade da Beira Interior, 6200-358 Covilha, Portugal

An in-house high-fidelity aerodynamic shape optimization computer program based on a computational fluid dynamics solver with the Spalart–Allmaras turbulence model and a sequential-quadratic-programming algorithm is used to obtain a set of optimal airfoils at the different flight conditions of a light unmanned air vehicle. For this study, the airfoil requirements at stall, takeoff run, climb gradient, rate of climb, cruise, and loiter conditions are obtained. Then, the aerodynamic shape optimization program is used to obtain the airfoil that has the optimal aerodynamic characteristics at each one of these flight conditions. Once the optimal airfoils at each flight condition are obtained, the results are analyzed to gain a better understanding of the most efficient initial airfoil configuration and the possible mechanisms that could be used to morph the single element airfoil. The results show that a very thin airfoil could be used as the initial configuration. Furthermore, a morphing mechanism that controls the camber and leading-edge thickness of the airfoil will almost suffice to obtain the optimal airfoil at most operating conditions. Lastly, the use of the optimal airfoils at the different flight conditions significantly reduces the installed power requirements, thus enabling a greater flexibility in the mission profile of the unmanned air vehicle.

Nomenclature

A	=	wing aspect ratio
b	=	wing span
C_D	=	three-dimensional drag coefficient
C_{D0}	=	aircraft parasite drag coefficient
C_{D0F}	=	aircraft less wing parasite drag coefficient
C_d	=	airfoil drag coefficient
C_{df}	=	airfoil friction drag coefficient
C_{dmin}	=	zerolift parasite drag coefficient of the wing
C_{dp}	=	airfoil pressure drag coefficient
C_L	=	three-dimentional lift coefficient
$C_{L\alpha}$	=	wing lift-curve slope
C_l	=	airfoil lift coefficient
C_{lmind}	=	lift coefficient at which C_{dmin} occurs
$C_{l\alpha}$	=	airfoil lift-curve slope
C_p	=	pressure coefficient
c	=	chord
d	=	fuselage diameter at wing intersection
e	=	Oswald coefficient
F	=	fuselage lift factor
g	=	gravity acceleration
h	=	altitude
i_w	=	wing/fuselage setting angle
K	=	induced grad coefficient factor
k	=	lift dependent parasite drag coefficient factor
P	=	power
P_0	=	sea-level engine power
RC	=	climb rate
Re	=	Reynolds number
S	=	wing reference area
S_{exp}	=	wing reference area excluding the area covered by the fuselage
t	=	airfoil thickness
V	=	speed
V_S	=	stall speed
v	=	ith design variable
v_{LE}	=	leading-edge design variable: defines the distance between the two control points at the leading edge
W	=	weight
x	=	horizontal coordinate, design variable
y	=	vertical coordinate
z	=	camber
α	=	airfoil angle of attack
α_f	=	fuselage angle of attack
α_w	=	wing angle of attack
α_0	=	zero-lift angle of attack
γ	=	climb angle
η_P	=	propeller propulsive efficiency
μ	=	air viscosity
μ_g	=	rolling friction coefficient
ρ	=	air density
ρ_0	=	air density at sea level

Presented as Paper 2005-1891 at the AIAA/ASME/ASCE/AHS/ASC 46th Structures, Structural Dynamics, and Materials Conference, Austin, TX, 18–21 April 2005; received 8 June 2005; revision received 16 November 2005; accepted for publication 19 December 2005.

*Ph.D. Student, Mechanical Engineering Department; secanell@uvic.ca.
†Professor, Mechanical Engineering Department; also Principal Investigator, Instituto de Engenharia Mecanica–Instituto Superior Tecnico, Av. Rovisco Pais 1, 1049-001 Lisbon, Portugal; suleman@uvic.ca. Associate Fellow AIAA.
‡Ph.D. Student, Aerospace Sciences Department; gamboa@demnet.ubi.pt.

I. Introduction

In recent years, the use of small unmanned aerial vehicles (UAVs) for aerial surveillance in various civil applications has been widely spread, because of its greater deployability when compared to conventional manned aircraft. Because of the UAV's potential for carrying out so many different tasks without direct risk to the crew or humans in general, they are ideal for testing new concepts that have been put forward as means to further increase the vehicle's capabilities. These concepts include not only new configurations and systems but also ways of changing the aircraft shape to better suit the mission profile.

New advances in smart materials and adaptive structures have made possible the idea of morphing airfoils or wing shapes in flight

to adapt the aircraft configuration to all flight conditions.[1–3] The goal is to create an airfoil or wing that will be able to reconfigure itself to give optimal performance at all flight conditions. For example, at the University of Notre Dame,[4,5] an UAV is being designed that will morph the airfoil in flight from a cruise low-drag configuration to a high-lift configuration at loiter speeds. The morphing mechanism is to split the airfoil into two airfoils to increase the wing area and, therefore, the lift.

In addition to all of the aforementioned advances, improvements in computational fluid dynamics and optimization have also increased the ability of engineers to improve the designs of aircraft. Since the late 1970s when Hicks and Henne[6] published one of the first papers on aerodynamic shape optimization, aerodynamic shape optimization has become a very active area of research, and several innovative methods for the aerodynamic shape optimization of airfoils,[7] wings,[8] full aircraft configurations,[9,10] and even aerostructural optimization of full aircraft configurations[11] have been published. In these papers, an aerodynamic shape optimization problem is solved to obtain a fixed optimal aircraft configuration. However, the new advances in morphing mechanisms allow aircraft performance to be further increased by obtaining the optimal aircraft configuration at different flight conditions and then use these morphing mechanisms to change aircraft configurations in flight in order to achieve an all-stage optimal performance.

In this paper, a high-fidelity aerodynamic shape optimization code is used to obtain a set of optimal airfoils at different flight conditions of a light UAV to gain insight on the most efficient initial airfoil configuration and the mechanisms to be used to morph a single element airfoil UAV. Section II describes the UAV characteristics and the different UAV flight conditions. From these data, the airfoil requirements are obtained. In Sec. III, an overview is given of the high-fidelity aerodynamic shape optimization tool used to obtain the set of optimal shapes. Section IV analyzes the results obtained from the optimization of the airfoils at the different flight conditions and outlines its main characteristics and how they affect the performance of the UAV. Finally, in the conclusions the results are analyzed in order to gain some insight into the necessary mechanisms for the development and construction of a morphing airfoil UAV and to quantify the advantages of having such a morphing capability.

II. Airfoil Requirements

In this section, realistic aerodynamic airfoil requirements for a light-surveillance UAV fitted with a morphing airfoil are obtained for its main flight conditions. The flight conditions used in this study are six: stall, takeoff run, climb gradient, rate of climb, cruise, and loiter. It is specified that the light-surveillance UAV requires a fast cruise to the surveillance area and back and a low-speed loiter on site.

A. UAV Characteristics

The main characteristics of the UAV are a takeoff weight W of 390 N, a constant chord c of 0.5 m across the span, and a wing area S of 1.4 m^2. From c and S one can calculate the wing span b and the wing aspect ratio A. Table 1 summarizes the UAV data. The weight in parentheses in Table 1 is the final weight of the UAV after the optimization calculations and after applying a weight correction to the wing to account for the reduction in airfoil thickness as given in Eq. (9), and the other value is the initial weight of the UAV.

The aerodynamic representation of the UAV assumes that only the wing contributes to lift, and it neglects fuselage drag and trim drag dependence on speed and angle of attack. The drag coefficient representation used is nonsymmetrical and is divided into three contributions: the wing parasite drag coefficient, the rest of the UAV parasite drag coefficient, and the induced drag coefficient. In this study, it is assumed that the airfoil used is typical for low-Reynolds-number Re applications, between 5×10^5 and 1.5×10^6, and that it is designed for a lift coefficient close to the expected lift coefficient value at the loiter phase. This airfoil exhibits a flat drag polar around the design lift coefficient. Thus, the aircraft drag polar is given by Eq. (1):

$$C_D = C_{D0} + KC_L^2 \tag{1}$$

where C_{D0} is the parasite drag coefficient given by

$$C_{D0} = C_{D0F} + C_{\text{dmin}} + k(C_l - C_{\text{lmind}})^4 \tag{2}$$

and K is given by

$$K = 1/(\pi Ae) \tag{3}$$

In the preceding two equations, C_{lmind} is the lift coefficient at which C_{dmin} occurs [this is equivalent to the airfoil drag coefficient, i.e., $C_d = C_{\text{dmin}} + k(C_l - C_{\text{lmind}})^4$, where the exponent 4 was found, by the authors, to give a better fit to the airfoil's experimental drag polar data points], C_{D0F} is the rest of the aircraft parasite drag coefficient, and C_l is the two-dimensional lift coefficient. The Oswald coefficient e is calculated from the empirical equation from Ref. 12:

$$e = 1.78(1 - 0.045A^{0.68}) - 0.64 \tag{4}$$

Table 2 summarizes the drag coefficients adopted for this study.

The UAV is assumed to use a small gasoline engine driving a fixed-pitch propeller, which can be optimized for a given speed. The propeller performance is highly dependent on the airspeed. A typical efficiency curve with a maximum of 0.75 at the propeller design speed of 50 m/s is given in Eqs. (5) and (6). These equations were obtained by fitting a sixth-order polynomial to the typical propeller propulsive efficiency curve given in Ref. 12. Better low-speed performance could be obtained by reducing the propeller design speed, provided means are available for limiting the engine rpm:

$$\eta_P = EV + GV^2 + HV^3 + IV^4 + JV^5 + MV^6 \tag{5}$$

where the coefficients of the polynomial are

$$\begin{aligned} E &= 2.6207810 \times 10^{-2}, & G &= -2.3493318 \times 10^{-4} \\ H &= 2.2835534 \times 10^{-6}, & I &= -1.5588826 \times 10^{-7} \\ J &= 4.0447704 \times 10^{-9}, & M &= -3.5238173 \times 10^{-11} \end{aligned} \tag{6}$$

Finally, it is likely that during the aerodynamic optimization process the airfoil thickness will vary. This, in turn, will affect the weight of the wing. Thus, a method is necessary to estimate the wing weight variation caused by the airfoil thickness. Based on Ref. 12, it is assumed that the weight of the wing is proportional to $(t/c)^{-0.3}$, where t/c is the relative thickness of the wing section and proportional to the aircraft total weight. Then, the new wing will have a weight of

$$W_{w2} = W_{w1}\left(\frac{W_2}{W_1}\right)\left[\frac{(t/c)_2}{(t/c)_1}\right]^{-0.3} \tag{7}$$

Table 1 Weight and geometric characteristics of the UAV

UAV data	Value
W, N	390 (400)
S, m^2	1.40
c, m	0.50
b, m	2.80
A	5.60

Table 2 Drag coefficient components of the UAV

Parameter	Value
C_{D0F}	0.0155
C_{dmin}	0.0080
k	0.0970
C_{lmind}	0.5000
e	0.8815
K	0.0645

Table 3 UAV requirements for the different flight conditions

Flight condition	V, m/s	h, m	ρ, kg/m^3	μ, 10^{-5} kg/ms	s_{TO}, m	V_{min}/V_S	μ_g	γ, deg	RC, m/s	V/V_S
Stall	18	0	1.225	1.786	——	——	——	——	——	——
Takeoff run	——	0	1.225	1.783	100	——	0.06	——	——	1.2
Climb gradient	——	0	1.225	1.783	——	1.2	——	9	——	——
Rate of climb	——	0	1.225	1.783	——	1.3	——	——	4	——
Cruise speed	50	2000	1.006	1.722	——	1.3	——	——	——	——
Loiter speed	20	2000	1.006	1.722	——	1.2	——	——	——	——

If the weight of the rest of the aircraft is not affected by the weight of the wing, then the new weight of the vehicle is given by

$$W_2 = W_1 - W_{w1} + W_{w2} \tag{8}$$

Assuming that the weight of the initial wing is 10% of the total initial aircraft weight and substituting Eq. (7) into Eq. (8), the weight of the final aircraft is, after some rearrangement, given by

$$W_2 = W_1 \left\{ \frac{0.9}{1 - 0.1[(t/c)_2/(t/c)_1]^{-0.3}} \right\} \tag{9}$$

B. Mission Requirements

A set of performance requirements for this UAV is used to determine the aerodynamic characteristics of the airfoil. The requirements are based on a typical mission for this type of light-surveillance UAV, but with a cruise speed, and loiter speed quite far apart, almost at opposite ends of the speed envelope. The requirements for stall speed, takeoff run distance, climb gradient, rate of climb, cruise speed, and loiter speed are given in Table 3. The variables in this table are as follows: V is the airspeed, V_S is the stall speed, V_{min} is the minimum operational speed, h is the altitude, ρ is the air density, μ is the air viscosity, s is the distance, μ_g is the rolling friction coefficient, γ is the climb angle, and RC is the rate of climb. A minimum safety speed is imposed on the speed requirements to prevent too low a speed to be adopted.

C. Airfoil Speed and Lift Requirement Analysis

The following analysis presents the equations for determining the appropriate C_L for each mission requirement, keeping in mind the need for minimizing the installed power. Except for the stall speed, the airfoil lift coefficient C_l is assumed to be the same as the wing lift coefficient.

It is assumed that the airfoil can be readily changed to the stall configuration so that the maximum lift coefficient at all times is the lift coefficient obtained in the stall speed requirement. Furthermore, the UAV weight is kept constant in all mission segments. The air density for each flight requirement is given in Table 3 and its variation with altitude affects the local stall speed.

Equations (10–22) were obtained from Ref. 12, either directly or after some rearranging.

1. Stall Speed

The maximum wing lift coefficient is given, for steady level flight, by the equation

$$C_{L\max} = \left(2/\rho V_S^2\right)(W/S) \tag{10}$$

and, assuming that the wing has no sweep and neglecting any wing/body effects, the airfoil maximum lift coefficient is approximated by

$$C_{l\max} = C_{L\max}/0.9 \tag{11}$$

2. Takeoff Run

The takeoff run distance is approximated by Eq. (12) assuming constant acceleration. This equation was obtained from Ref. 12 by expressing thrust in terms of power.

$$s_{TO} = W V_{TO}^2 \Big/ 2g \left[\frac{\eta_{Pav}(\rho/\rho_0) P_0}{V_{TOav}} - \frac{1}{2}\rho V_{TOav}^2 S\left(C_{D0} - \mu_g C_L + K C_L^2\right) - \mu_g W \right] \tag{12}$$

where the average propeller efficiency η_{Pav} is calculated at the average speed V_{TOav} given by

$$V_{TOav} = \frac{V_{TO}}{\sqrt{2}} = \frac{(V/V_S)_{TO} V_S}{\sqrt{2}} = \left(\frac{V}{V_S}\right)_{TO} \sqrt{\frac{1}{\rho C_{L\max}}\left(\frac{W}{S}\right)} \tag{13}$$

In Eq. (12), P_0 and ρ_0 are the engine maximum power and the air density at sea level, international standard atmosphere, respectively. Substituting for V_{TOav} in Eq. (12) and solving for the power-to-weight ratio, one obtains the following expression:

$$\left(\frac{\rho}{\rho_0}\right)\left(\frac{P_0}{W}\right) = \frac{(V/V_S)_{TO}}{\eta_{Pav}\sqrt{\rho C_{L\max}}} \sqrt{\frac{W}{S}} \left\{ \frac{(V/V_S)_{TO}^2}{2C_{L\max}} \left[\frac{2}{\rho g s_{TO}} \left(\frac{W}{S}\right) + \left(C_{D0} - \mu_g C_L + K C_L^2\right) \right] + \mu_g \right\} \tag{14}$$

From Eq. (14) it can be seen that, given the takeoff run distance, aircraft characteristics, and runway altitude, the power required can be minimized by maximizing $C_{L\max}$ and minimizing $(C_{D0} - \mu_g C_L + K C_L^2)$. Because the maximum lift coefficient has been determined, the latter expression is minimized with respect to C_L giving

$$C_L = \mu_g / 2K \tag{15}$$

Equation (15) gives the required lift coefficient during the takeoff run condition if the required installed power is to be minimized.

3. Climb Gradient

The power-to-weight ratio in a steady climb as a function of the climb angle is derived from the equations in Ref. 12 to be

$$\left(\frac{\rho}{\rho_0}\right)\left(\frac{P_0}{W}\right) = \frac{1}{\eta_P}\left[V \sin\gamma + \frac{\rho C_{D0}}{2(W/S)} V^3 + \frac{2K}{\rho}\left(\frac{W}{S}\right) V^{-1} \right] \tag{16}$$

Note that in this equation η_P is a function of V as seen in Eq. (5). The speed, for a given climb angle, that minimizes the required installed power is obtained by numerically varying the speed until a minimum is reached. This speed might be too close to the stalling speed. Thus, in normal aerial operations one flies at or above a minimum safety speed, usually $1.2V_S$ after takeoff, given by

$$V_{min} = \left(\frac{V_{min}}{V_S}\right) V_S = \left(\frac{V_{min}}{V_S}\right) \sqrt{\frac{2}{\rho C_{L\max}}\left(\frac{W}{S}\right)} \tag{17}$$

When calculating V_{min}, the ratio V_{min}/V_S is taken from Table 3 from the appropriate requirement. The speed adopted V, which minimizes the installed power while maintaining a safety speed, is the higher of the speed obtained by minimizing Eq. (16) and the speed

Table 4 Speed requirements

Speed, m/s	Stall	Takeoff run	Climb gradient	Climb rate	Cruise	Loiter
Minimum safety	——	——	21.600	23.400	25.822	23.835
Minimum power	——	——	24.000	31.333	28.667	28.667
Maximum range	——	——	——	——	35.333	——
Specified	18.000	——	——	——	50.000	20.000
Adopted	18.000	15.274	24.000	31.333	50.000	23.835

given by Eq. (17). Once the speed is obtained, the lift coefficient in climbing flight is obtained from Eq. (18):

$$C_L = (2/\rho V^2)(W/S)\cos\gamma \tag{18}$$

The selected flight speed results in a lift coefficient that minimizes the required installed power for this requirement while satisfying a minimum safety speed.

4. Climb Rate

The power-to-weight ratio in a steady climb as a function of the rate of climb is given by[12]

$$\left(\frac{\rho}{\rho_0}\right)\left(\frac{P_0}{W}\right) = \frac{1}{\eta_P}\left[\mathrm{RC} + \frac{\rho C_{D0}}{2(W/S)}V^3 + \frac{2K}{\rho}\left(\frac{W}{S}\right)V^{-1}\right] \tag{19}$$

Again, the speed for a given rate of climb that minimizes the required installed power is obtained by numerically varying the speed until a minimum is reached. The minimum safety speed is given by Eq. (17). The speed adopted V is the higher of the speed obtained by minimizing Eq. (19) and the speed given by Eq. (17). The lift coefficient in climbing flight is obtained from Eq. (18) where the climb angle is given by Eq. (20):

$$\sin\gamma = \mathrm{RC}/V \tag{20}$$

The obtained lift minimizes the required installed power while satisfying a minimum safety speed.

5. Cruise Speed

The power-to-weight ratio in steady level flight is given by[12]

$$\left(\frac{\rho}{\rho_0}\right)\left(\frac{P_0}{W}\right) = \frac{1}{\eta_P}\left[\frac{\rho C_{D0}}{2(W/S)}V^3 + \frac{2K}{\rho}\left(\frac{W}{S}\right)V^{-1}\right] \tag{21}$$

The cruise speed is typically higher than the minimum installed power speed or the best range speed because these are usually quite low. The speed that would minimize the required installed power is, again, obtained by numerically varying the speed until a minimum is reached. The maximum range speed can be obtained from the Breguet range equation[12] by numerically varying the speed until the ratio $\eta_P C_L/C_D$ is maximized, assuming the engine specific fuel consumption to be constant. The minimum safety speed for cruise is given by Eq. (17). The minimum speed is used as a means to prevent too low a speed to be adopted by the analysis if, for instance, the minimum power speed or the specified speed are below it. One could use the maximum range speed in this analysis, but, as already stated, the requirements ask for a high speed to reduce the time to reach the surveillance zone.

The adopted cruise speed V is the higher of the speed obtained by minimizing Eq. (21), the speed given by Eq. (17), the maximum range speed, and the specified cruise speed. Using the computed cruise speed, the lift coefficient that minimizes the installed power of the UAV in steady level flight is obtained from

$$C_L = (2/\rho V^2)(W/S) \tag{22}$$

6. Loiter Speed

The power-to-weight ratio in steady level flight is given by Eq. (21). The minimum installed power speed is obtained by minimizing this equation with respect to V. The minimum safety speed is given by Eq. (17).

The speed adopted, in this case, is the higher of the speed given by Eq. (17) and the specified loiter speed. The minimum installed power speed was not used because a lower speed than the one obtained in this condition is preferred in the surveillance phase to reduce the ground speed over a specified ground target. The lift coefficient in level flight is given by Eq. (22).

Table 4 shows the results from the preceding analysis. When calculating these speeds, the value used for the weight of the UAV was 400 N because after the airfoil optimization the airfoil relative thickness reduced from 10 to 5%, which resulted in a 10-N increase in the wing weight.

D. Airfoil Angle-of-Attack Requirement Analysis

To have the complete set of airfoil requirements, it is also necessary to calculate the airfoil angle of attack (AOA). This angle of attack could be varied during the shape optimization process in conjunction with all other shape variables. However, to obtain accurate results, the angle of attack of the airfoil must be related to the angle of attack of wing and fuselage. These are not modeled in the computational fluid dynamics (CFD) solver, and therefore, drag predictions will be inaccurate. Furthermore, from an optimization point of view, because of the different magnitude and nature of this design variable the introduction of this variable into the design process leads to an optimization problem for which the methods used in this paper were not able to achieve a converged solution. For these reasons, in this paper the authors decided to vary only the shape of the airfoil. The introduction of angle of attack as well as the flight speed into the design process can further improve the performance of the morphing UAV; however, because of the added complexity it is outside the scope of this work, and it will be studied only in future publications.

The wing lift-curve slope for a straight rectangular wing with no twist which airfoil section has a lift-curve slope of 2π can be obtained at very low Mach numbers from the semiempirical formula[12]

$$C_{L\alpha} = \left[2\pi A \Big/ \left(2 + \sqrt{4 + A^2}\right)\right](S_{\exp}/S)F \tag{23}$$

where $S_{\exp}$ is the exposed wing area, that is, the wing platform reference area less the part of the wing covered by the fuselage and F is the fuselage lift factor given by[12]

$$F = 1.07(1 + d/b)^2 \tag{24}$$

where d is the fuselage diameter where the wing intersects the fuselage. For the wing geometry given in Table 1 and assuming a fuselage diameter of 0.3 m, the lift-curve slope of the wing is 4.4279 rad^{-1}.

The lift coefficient of the wing is calculated from

$$C_L = C_{L\alpha}(\alpha_w - \alpha_0) = C_{L\alpha}(\alpha_f + i_w - \alpha_0) \tag{25}$$

The angles of attack for the airfoil that give the required lift coefficients are estimated using the thin airfoil theory, which does not take any viscous effects into consideration. This theory states that the lift-curve slope of the thin airfoil is 2π and that the lift coefficient is given by

$$C_l = 2\pi(\alpha - \alpha_0) \tag{26}$$

Table 5 Wing AOA requirements

Parameter	Stall	Takeoff run	Climb gradient	Climb rate	Cruise	Loiter
C_l	1.5997	0.4653	0.7999	0.4751	0.2272	0.9998
C_L	1.4397	0.4653	0.7999	0.4751	0.2272	0.9998
α_f, deg	6.0000	0.0000	0.0000	0.0000	0.0000	0.0000
α_w, deg	8.0000	2.0000	2.0000	2.0000	2.0000	2.0000
α_0, deg	−10.6298	−4.0209	−8.3505	−4.1477	−0.9399	−10.9372

Table 6 Airfoil design requirements for each flight condition

Parameter	Stall	Takeoff run	Climb gradient	Climb rate	Cruise	Loiter
V, m/s	18.000	15.274	24.000	31.333	50.000	23.835
ρ, kg/m^3	1.225	1.225	1.225	1.225	1.006	1.006
Re	618.34×10^3	524.679×10^3	824.853×10^3	$1{,}076.369 \times 10^3$	$1{,}460.511 \times 10^3$	696.238×10^3
$C_l^{\min}$	1.5997	0.4653	0.7999	0.4751	0.2272	0.9998
α, deg	6.0000	0.2222	−1.0563	0.1847	1.1319	−1.8201
C_d	Minimize	Minimize	Minimize	Minimize	Minimize	Minimize

where the zero-lift AOA is a function of the shape of the airfoil camber line. Knowing that the zero-lift angle of the airfoil is the same as that of the wing, the required airfoil angle of attack is obtained by solving Eq. (26) with respect to α.

For the UAV under consideration, one requires low aerodynamic drag in most of its mission phases. This can be achieved by placing the fuselage at zero AOA to the airflow. This is done for cruise, loiter, climb, and takeoff run. Thus, in these conditions $\alpha_f = 0$ deg, and a wing incidence i_w of 2 deg is adopted because typical wing/fuselage setting angles range from 0 to 2 deg as discussed in Ref. 12. For the stall condition an AOA of 6 deg is chosen.

With these values and using Eq. (25), the required zero-lift AOA for all flight conditions is obtained. The results are shown in Table 5, where C_L is obtained from the analysis in subsection II.C for the corresponding speed from Table 4 and air density from Table 3. Note that $C_l = C_L$ for all conditions except for stall where the wing lift coefficient is obtained using Eq. (11). From the zero-lift AOA values in Table 5, it can be observed that there are four basic airfoil camber lines for this UAV: one for stall and loiter, one for takeoff run and rate of climb, one for climb gradient, and another for cruise.

E. Airfoil Aerodynamic Requirements

Using the mission requirements of Table 3, the aerodynamic requirements for the morphing airfoil are shown in Table 6. Because the analysis just carried out does not consider viscous effects, it might be necessary to increase the AOA for the stall requirement in order to obtain the desired lift coefficient. A suggestion is to add 2 deg to the value given by Eq. (26), that is, $\alpha = 6$ deg, because the stall angle of attack of common airfoils occurs 2–4 deg above the AOA at the linear lift-curve intersection with the maximum lift coefficient value as represented in Fig. 1. The airfoil drag coefficient C_d must be minimized in all conditions for the required power to be minimized.

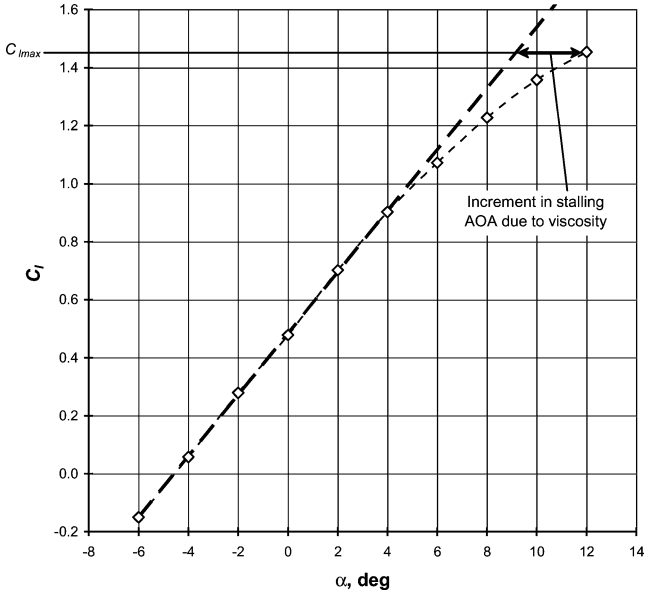

Fig. 1 Difference in maximum AOA between linear and real lift curves: ◇, typical curve and – – –, linear curve.

III. Aerodynamic Optimization

Once the airfoil requirements for each airfoil have been specified, the optimal airfoil for each flight condition needs to be obtained by using a shape optimization solver. Several steps are required to solve an airfoil shape optimization problem: the airfoil must be mathematically defined in such a way that it is possible to change its shape; a method must be implemented to account for the deformation of the airfoil in the fluid mesh used by the CFD solver; a CFD solver must be selected to obtain the necessary values to compute the objective function and constraints; a method must be chosen to compute the gradients; and finally an optimization algorithm must be used. In the following paragraphs, the different methods selected for each step are described.

The shape of the airfoil is represented mathematically as a B-spline. A B-spline is chosen because it provides a wide variety of airfoil shapes using a small number of design variables (i.e., the vertical location of the B-spline control points can be used as the design variables). It also guarantees localized shape changes of the airfoil when a design variable is perturbed. These characteristics are highly desirable when solving the optimization problem. In particular, for this paper the airfoils are represented using a B-spline with 15 control points. From these 15 control points, 11 are used as design variables. In particular, the control points numbered from 1 to 5 and from 7 to 11 on Fig. 2 are used as design variables. Furthermore, the distance between the two control points at the leading edge is also used as a design variable. This variable is used to control the shape of the leading edge during optimization.

The required drag and lift coefficients are obtained using a viscous parallel solver, namely, the Structured Parallel Research Code (SPARC).[13] After the lift and drag coefficients are obtained, the value of the objective function and constraints is computed.

The gradients of the objective function and constraints are a requirement of any gradient-based optimization algorithm. In this work, the gradients are computed using finite differences. Using finite differences enables the problem of finding the gradients to be treated as a black box, and therefore it can be used with any fluid flow solver because it does not involve changes in the solver's code. Additionally, it is very easy to implement, and it is easy to parallelize.

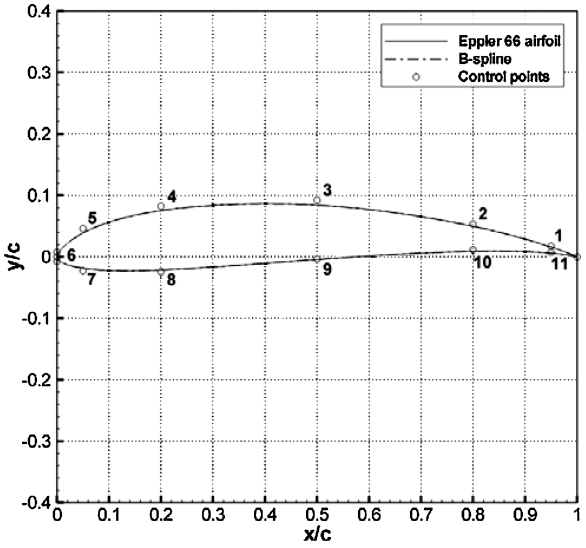

Fig. 2 B-spline representation of the Eppler 66 airfoil.

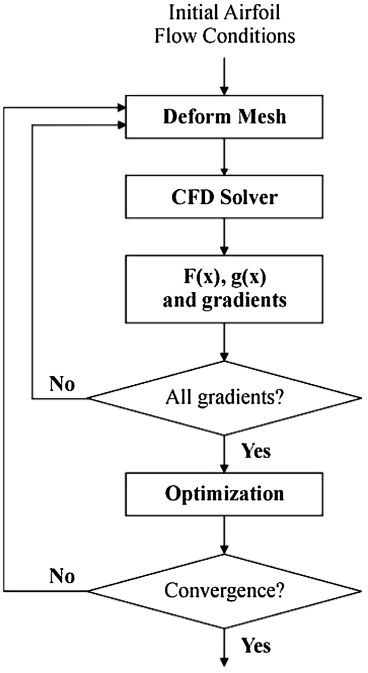

Fig. 3 Flowchart of the aerodynamic shape optimization design tool.

Once the objective function, the constraints, and their gradients are computed, an optimization algorithm is used to obtain an improved airfoil shape. The optimization algorithm used here is the sequential-quadratic-programming (SQP) method implemented in DOT.[14] The SQP method has been proven to yield good results when solving aerodynamic shape optimization problems at low Reynolds numbers.[15,16]

Finally, the original airfoil needs to be deformed into the new airfoil given by the optimization algorithm for the lift and drag coefficients for the new airfoil to be computed. The deformations of the airfoil are accounted for in the fluid flow solver by deforming the fluid mesh using transfinite interpolation together with a spring network approach.[17] If the new airfoil meets the design requirements, the algorithm stops. If the new airfoil does not meet the design requirements, the process just described continues iteratively until an airfoil is found that meets the convergence criteria. This process is summarized in a flowchart in Fig. 3, and it is described in detail in Ref. 18.

IV. Results and Discussion

The results are presented in two parts: the first contains the airfoil design optimization results, whereas the second contains the power requirement results for the UAV before and after airfoil optimization. This work deals only with aerodynamic shape optimization; no structural considerations were implemented in the design, except for a minimum thickness of approximately 1 and 5% of the chord at the leading- and trailing-edge points and the center points, respectively.

A. Airfoil Design Optimization Results

For the stall, takeoff run, climb gradient, rate of climb, cruise and loiter flight conditions, the airfoil shape is obtained by solving a minimum drag airfoil optimization problem subject to a minimum lift coefficient requirement and several thickness constraints.

Minimize:

$$\underset{\text{w.r.t.: } v_i}{} \quad c_d$$

Subject to:

$$c_l \geq c_l^{\text{desired}}$$

$$v_1 - v_{11} \geq 0.01c$$

$$v_2 - v_{10} \geq 0.01c$$

$$v_3 - v_9 \geq 0.05c$$

$$v_4 - v_8 \geq 0.05c$$

$$v_5 - v_7 \geq 0.01c$$

$$v_{\text{LE}} \geq 0.01c$$

This method is used because, given a specific speed requirement at each flight requirement, minimizing the drag and keeping the lift equal to the weight of the aircraft will minimize the power necessary from the propulsive system. This will increase the range and efficiency of the vehicle. Notice that in this case, because the lift is set constant, that is, equal to the weight, minimizing the drag is equivalent to maximizing range or endurance because maximizing the inverse of a function times a constant is equivalent to minimizing the function itself. In the problem statement the lift constraint is expressed as an inequality constraint. This improves the performance of the optimization algorithm without compromising the results because an equality constraint will yield the same result because lift and drag are opposing goals. Furthermore, the constraints used to limit the minimum thickness of the airfoil are set for completeness because these constraints should be obtained using a structural solver.

To solve the optimization problems, the Eppler 66 airfoil, which is a typical airfoil for low-Reynolds-number applications, is used as the initial airfoil. The aerodynamic characteristics of the airfoil are obtained using SPARC and the grid shown in Fig. 4. The validity of this grid was proven by Secanell[16,18] by developing an extensive grid study; therefore, no other grid study is undertaken in this paper.

1. *Stall Speed*

In the first condition, the stall, the design tool reached the optimal airfoil after seven iterations: seven gradient evaluations and 17 internal function evaluations, adding up to a total of 101 function evaluations. At the end of the optimization, the airfoil satisfies all aerodynamic and geometric constraints as shown in Table 7 and Fig. 5. The optimal airfoil has the required lift coefficient of 1.59975 and a drag coefficient of 1.70429×10^{-2}. The initial design was an infeasible one because the lift coefficient was less than the minimum required lift coefficient. The new airfoil design shows a 25% increase in the lift coefficient and a 9.3% increase in the drag coefficient. This results in an important increase in the lift-to-drag ratio (L/D) of 14.3%. From Table 7, it can be seen that the increase in the drag coefficient is mainly caused by the 12.4% increase in the pressure drag coefficient C_{dp}. This increase in the pressure drag is because of the change in the airfoil geometry, which resulted in a higher pressure along the lower surface and an increase in the leading-edge low-pressure peak as shown in Fig. 6. Because the

Table 7 Aerodynamic characteristics of the initial and optimal airfoils at stall conditions, $Re = 618.340 \times 10^3$ and $\alpha = 6.0000$ deg

Parameter	Eppler 66 (stall)	UAV (stall)
C_l	1.27996	1.59975
$C_d \times 10^2$	1.55989	1.70429
$C_{\mathrm{df}} \times 10^2$	0.45180	0.45914
$C_{\mathrm{dp}} \times 10^2$	1.10809	1.24515
L/D	82.0545	93.8661

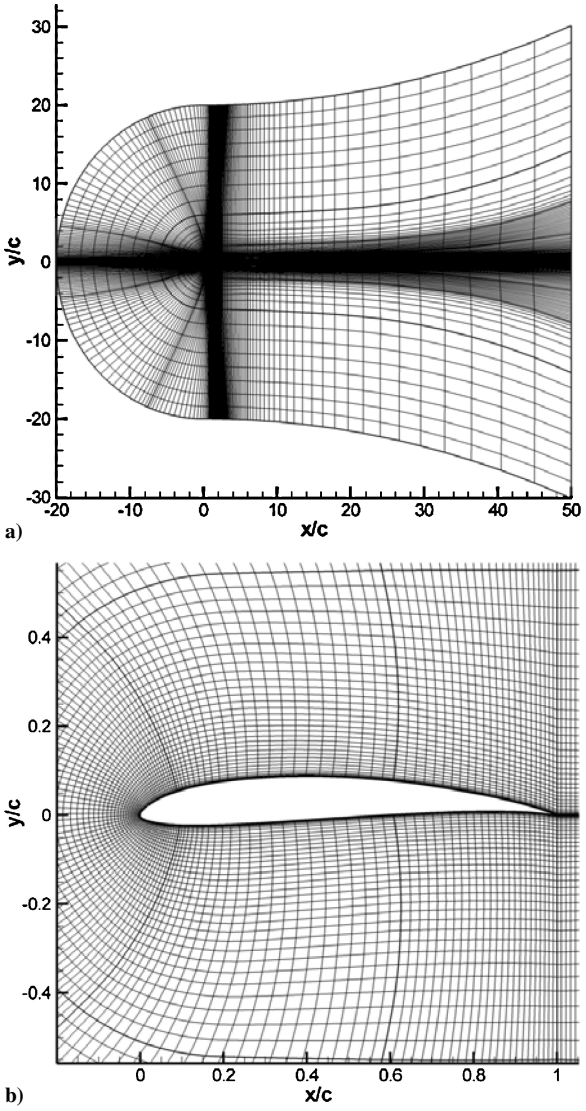

Fig. 4 Grid used for the optimization algorithm: a) complete grid and b) detail of the grid around the airfoil.

airfoil is placed at 6-deg AOA to the flow direction, the pressure drag coefficient had to increase for the lift to increase. On the other hand, the friction drag coefficient C_{df} is essentially unchanged. From Figs. 5 and 7, it can be observed that the airfoil camber increased by a large amount, reaching its maximum in this flight condition, but its thickness decreased aft of 5% of the chord. The new camber line shape with its increased maximum value is required to produce the high lift coefficient required, whereas the thickness reduction in such a manner is the means to avoid the drag coefficient to increase too much.

2. Takeoff Run

In the takeoff run case, the design tool reached the optimal airfoil after 11 iterations: 11 gradient evaluations and 33 internal function evaluations, adding up to a total of 165 function evaluations.

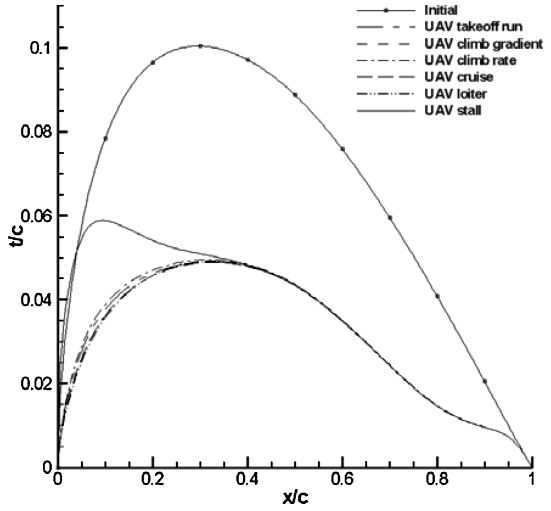

Fig. 5 Thickness distribution of the initial airfoil and the optimal airfoils at each flight condition.

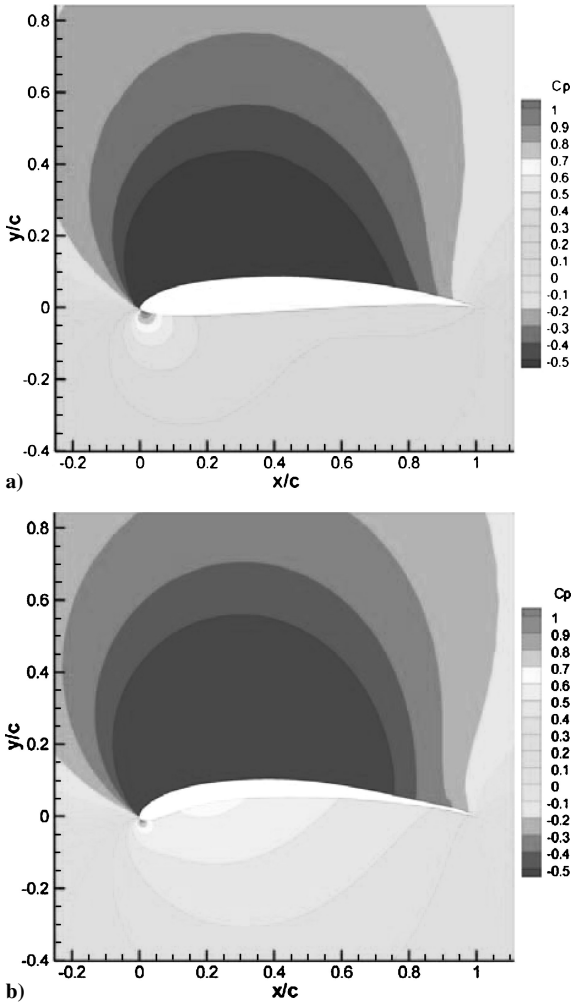

Fig. 6 Pressure coefficient contours of the a) initial airfoil and the b) optimal airfoil at stall conditions, $Re = 618.340 \times 10^3$ and $\alpha = 6.0000$ deg.

At the end of the optimization, the airfoil satisfies all aerodynamic and geometric constraints as shown in Table 8 and Fig. 5. The optimal airfoil has the required lift coefficient of 0.46530 and a drag coefficient of 0.64727×10^{-2}. The initial design, in this case, was feasible, as can be observed from the lift coefficient values in Table 8. Comparing the results of the initial and final airfoils, it is observed a 31% reduction in the lift coefficient and a 22.6% reduction in the drag coefficient, both reductions being very similar. From

Table 8 Aerodynamic characteristics of the initial and optimal airfoils at takeoff run conditions, $Re = 524.679 \times 10^3$, and $\alpha = 0.2222$ deg

Parameter	Eppler 66 (takeoff run)	UAV (takeoff run)
C_l	0.67790	0.46530
$C_d \times 10^2$	0.83612	0.64727
$C_{\mathrm{df}} \times 10^2$	0.50210	0.47864
$C_{\mathrm{dp}} \times 10^2$	0.33402	0.16863
L/D	81.0769	71.8865

Table 9 Aerodynamic characteristics of the initial and optimal airfoils at climb gradient conditions, $Re = 824.853 \times 10^3$ and $\alpha = -1.0563$ deg

Parameter	Eppler 66 (climb gradient)	UAV (climb gradient)
C_l	0.54130	0.79990
$C_d \times 10^2$	0.69303	0.71383
$C_{\mathrm{df}} \times 10^2$	0.42500	0.43392
$C_{\mathrm{dp}} \times 10^2$	0.26803	0.27991
L/D	78.1063	112.0575

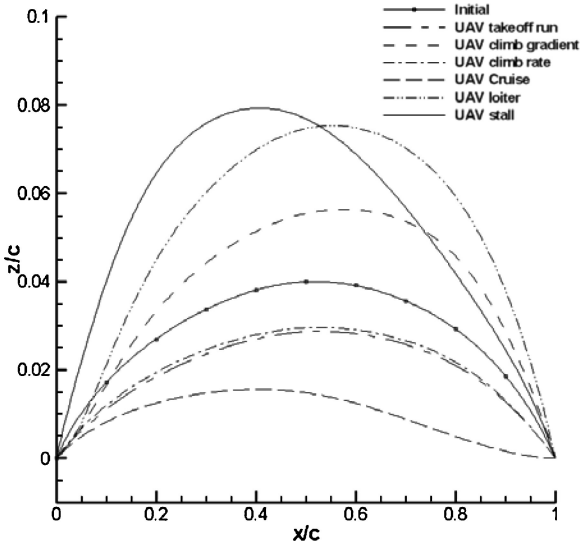

Fig. 7 Camber lines of the initial airfoil and the optimal airfoils at each flight condition.

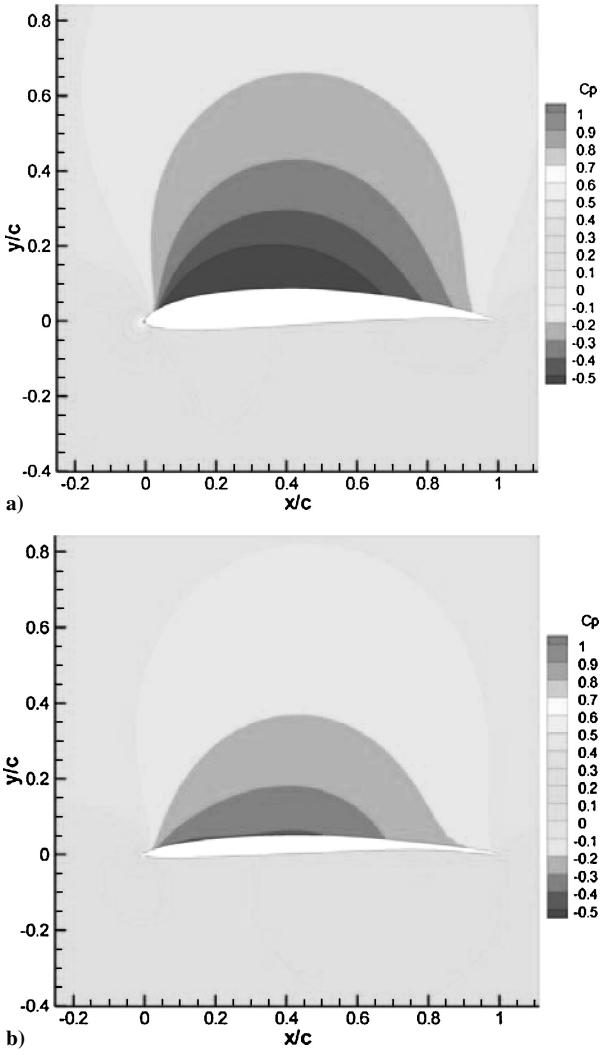

Fig. 8 Pressure coefficient contours of the a) initial airfoil and the b) optimal airfoil at takeoff run conditions, $Re = 524.679 \times 10^3$ and $\alpha = 0.2222$ deg.

Table 8, it can be seen that the decrease in the drag coefficient is mainly caused by the 49.5% decrease in the pressure drag coefficient. This decrease in pressure drag is caused by the change in the airfoil geometry and also to the reduced region of high pressure at the leading edge as shown in Fig. 8. On the other hand, the friction drag coefficient is only slightly reduced. The friction drag coefficient depends on the surface shear stress and on the airfoil wetted area. In this case, it seems that the shear stress reduced as a result of the lower adverse pressure gradients on the upper surface. The wetted area also reduced. These two factors combined led to the reduction in the friction drag coefficient. From Figs. 5 and 7, it can be observed that the airfoil camber reduced by a small amount, but its thickness greatly decreased helping in the reduction of pressure and friction drag coefficients. The camber reduction is required to lower the lift coefficient at the same AOA, whereas the reduced thickness allowed for the reduction of the drag coefficient.

3. Climb Gradient

For the climb gradient conditions, the design tool reached the optimal airfoil after 10 iterations: 10 gradient evaluations and 27 internal function evaluations, adding up to a total of 147 function evaluations. The initial airfoil was an infeasible design. At the end of the optimization, the airfoil satisfies all aerodynamic and geometric constraints as shown in Table 9 and Fig. 5. The optimal airfoil has the required lift coefficient of 0.79990 and a drag coefficient of 0.71383×10^{-2}. This represents a 48% increase in the lift coefficient and a 3% increase in the drag coefficient. In this case, the drag coefficient is slightly increased. This was necessary to satisfy the lift coefficient constraint because lift and drag are essentially opposing goals and the initial airfoil had a lower lift coefficient than the minimum lift required. However, the drag coefficient increased by a small amount when compared to the substantial increase in the lift coefficient. Table 9 shows that the increase in drag is mainly caused by an increase in pressure drag, as it was in the stall condition. This increase in pressure drag is caused by the change in the airfoil geometry and the resulting new pressure distribution whose low pressure peak on the upper surface moved downstream as shown in Fig. 9. The friction drag coefficient slightly increases, probably because of the increased pressure gradient toward the trailing edge, which results in an increased friction coefficient. From Fig. 7, it can be observed that the camber increased and that the maximum camber occurs at a position just in front of 60% of the chord. This increase in camber was necessary to give the high lift coefficient at the required low design AOA, which is just below zero.

4. Climb Rate

In the rate-of-climb case, the design tool reached the optimal airfoil after nine iterations: nine gradient evaluations and 24 internal function evaluations, adding up to a total of 132 function evaluations. At the end of the optimization, the airfoil satisfies all aerodynamic

Table 10 Aerodynamic characteristics of the initial and optimal airfoils at climb rate conditions, $Re = 1{,}076.369 \times 10^3$ and $\alpha = 0.1847$ deg

Parameter	Eppler 66 (climb rate)	UAV (climb rate)
C_l	0.68760	0.47510
$C_d \times 10^2$	0.67907	0.52858
$C_{\mathrm{df}} \times 10^2$	0.39900	0.38130
$C_{\mathrm{dp}} \times 10^2$	0.28007	0.14728
L/D	101.2561	89.8823

Table 11 Aerodynamic characteristics of the initial and optimal airfoils at cruise conditions, $Re = 1{,}460.511 \times 10^3$ and $\alpha = 1.1319$ deg

Parameter	Eppler 66 (cruise)	UAV (cruise)
C_l	0.80040	0.22721
$C_d \times 10^2$	0.66819	0.43669
$C_{\mathrm{df}} \times 10^2$	0.35610	0.33385
$C_{\mathrm{dp}} \times 10^2$	0.31209	0.10284
L/D	119.7863	52.0300

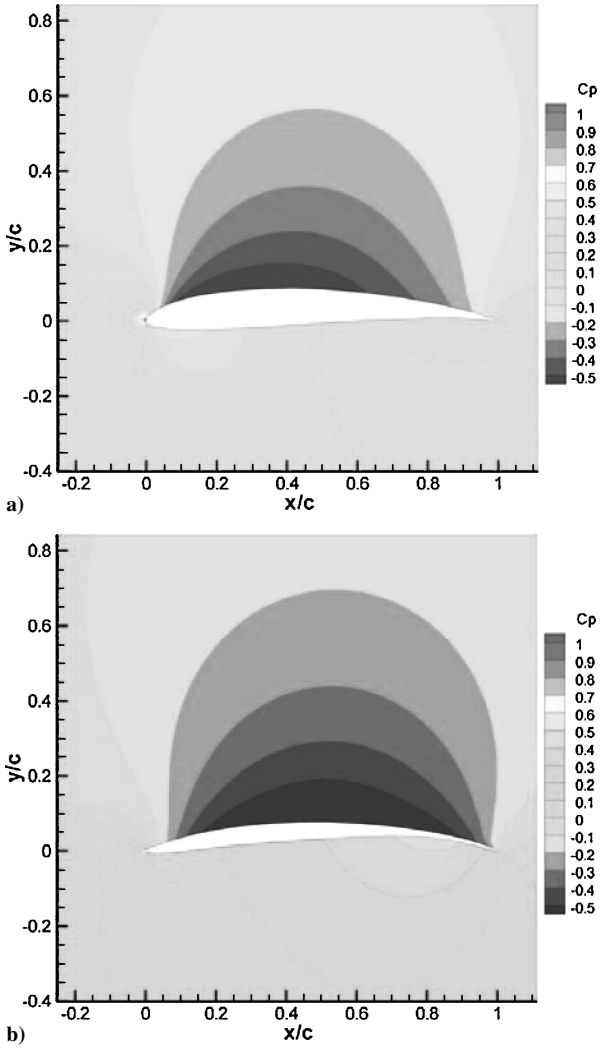

Fig. 9 Pressure coefficient contours of the a) initial airfoil and the b) optimal airfoil at climb gradient conditions, $Re = 824.853 \times 10^3$ and $\alpha = -1.0563$ deg.

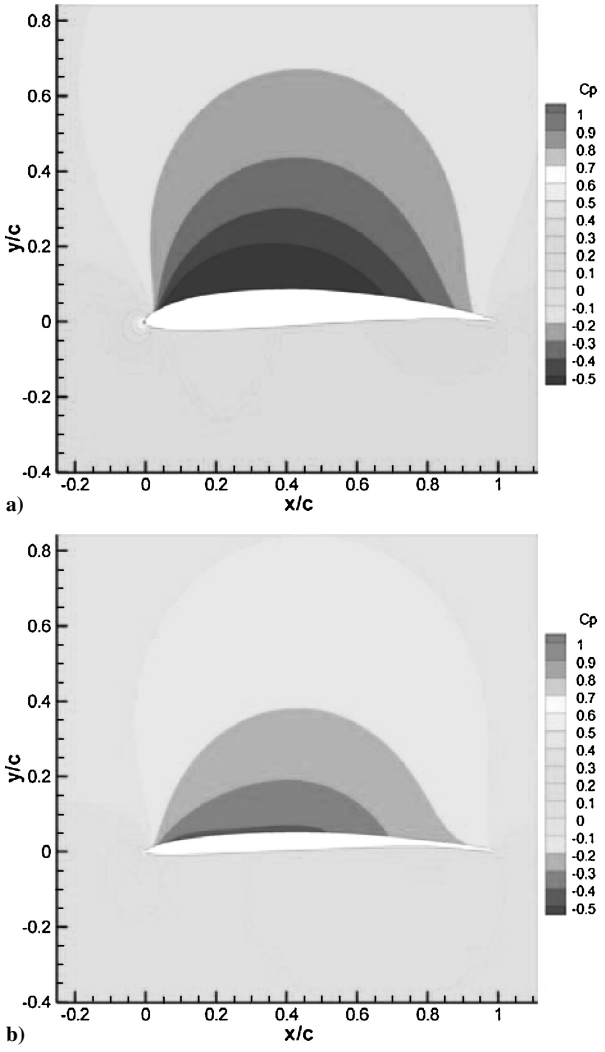

Fig. 10 Pressure coefficient contours of the a) initial airfoil and the b) optimal airfoil at climb rate conditions, $Re = 1{,}076.369 \times 10^3$ and $\alpha = 0.1847$ deg.

and geometric constraints as shown in Table 10 and Fig. 5. The optimal airfoil has the required lift coefficient of 0.47510 and a drag coefficient of 0.52858×10^{-2}. This represents a reduction of 31% in the lift coefficient and a reduction of 22% in the drag coefficient. Looking at Table 10, it can be seen that the reduction in drag is mainly caused by a reduction in pressure drag. This reduction in pressure drag is caused by the change in geometry and also to a reduction of the high-pressure region on the leading edge as happened in the takeoff run case. This is seen in Fig. 10. Again, the friction drag coefficient remains fairly unchanged, and it is even reduced as a result of the reduced adverse pressure gradients and the reduced wetted area. From Fig. 7, it can be observed that the camber line shape remained almost unchanged, though reducing its maximum value slightly, and that the maximum camber occurs at about mid-chord position. The camber in this airfoil is very similar to that of the takeoff run airfoil.

5. Cruise Speed

For the cruise conditions, the design tool reached the optimal airfoil after 10 iterations: 10 gradient evaluations and 25 internal function evaluations, adding up to a total of 145 function evaluations. The design tool obtained an airfoil with a drag coefficient of 0.43669×10^{-2}; this is a reduction of 34.5% with respect to the initial design. The drag reduction is mainly caused by a 67% reduction in the pressure drag. The large reduction is obtained by reducing the low-pressure region over the aft part of the airfoil and by reducing the high-pressure region at the leading edge as can be seen in Fig. 11. The friction drag is also reduced as seen from Table 11, but by a smaller amount, because the shear stress at the airfoil boundary is more difficult to reduce. The shape of the airfoil is plotted in Fig. 11. Comparing the original and final airfoils, it can be observed that the reduction in drag results from a reduction in camber, a reduction in the thickness, and changes in the leading-edge shape of the airfoil.

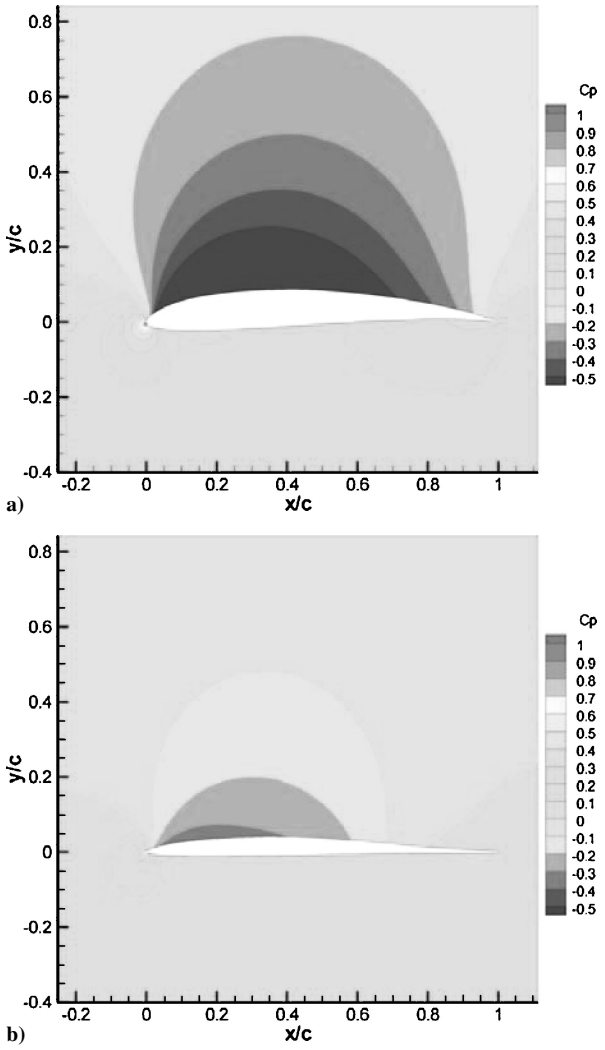

Fig. 11 Pressure coefficient contours of the a) initial airfoil and the b) optimal airfoil at cruise conditions, $Re = 1{,}460.511 \times 10^3$ and $\alpha = 1.1319$ deg.

This demonstrates that the optimization algorithm seeks a reduction in drag by reducing the thickness of the airfoil, except at the leading edge where the reduction of the pressure gradient is more important in order to guarantee that the boundary layer remains attached by maintaining low-pressure gradients. The camber is reduced, and its maximum moved forward to about 40% of the chord.

6. Loiter Speed

In the loiter case, the design tool reached the optimal airfoil after 10 iterations: 10 gradient evaluations and 25 internal function evaluations, adding up to a total of 145 function evaluations. The initial airfoil was an infeasible design. At the end of the optimization, the airfoil satisfies all aerodynamic and geometric constraints as shown in Table 12 and Fig. 5. The optimal airfoil has the required lift coefficient of 0.99958 and a drag coefficient of 0.9096×10^{-2}. This represents an increase of 122% in the lift coefficient and an increase of 26% in the drag coefficient. In this case, the drag coefficient is increased. However, the drag coefficient increased by a small amount when compared to the substantial increase in the lift coefficient. From Table 12, it can be seen that the increase in the drag coefficient is mainly caused by an increase in pressure drag. This increase in pressure drag is caused by the change in geometry, which forced the low-pressure peak to move downstream creating a larger region of low pressure at the upper back of the airfoil as shown in Fig. 12. On the other hand, the friction drag coefficient remains fairly unchanged, and it is slightly increased. From Fig. 5, it can be observed that the camber increased and that the maximum

Table 12 Aerodynamic characteristics of the initial and optimal airfoils at loiter conditions, $Re = 696.238 \times 10^3$ and $\alpha = -1.8201$ deg

Parameter	Eppler 66 (loiter)	UAV (loiter)
C_l	0.45070	0.99958
$C_d \times 10^2$	0.72103	0.90960
$C_{\mathrm{df}} \times 10^2$	0.43700	0.46630
$C_{\mathrm{dp}} \times 10^2$	0.28403	0.44330
L/D	62.5078	109.8923

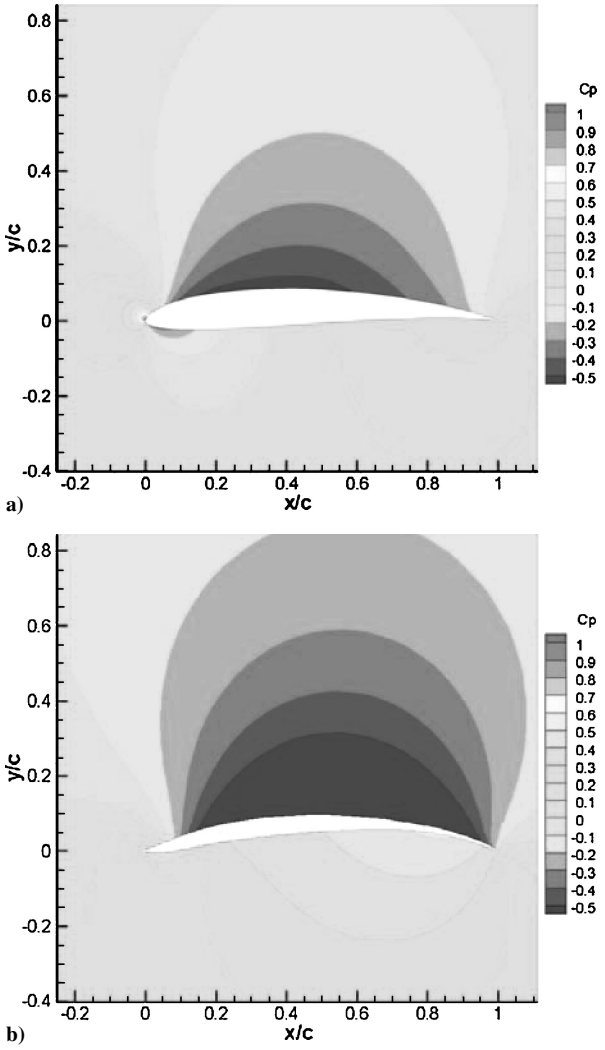

Fig. 12 Pressure coefficient contours of the a) initial airfoil and the b) optimal airfoil at loiter conditions, $Re = 696.238 \times 10^3$ and $\alpha = -1.8201$ deg.

camber occurs slightly behind the midchord position. Again, the thickness reduced to almost the minimum allowed as seen in Fig. 5.

In all of the preceding flight conditions, the design tool tried to reduce the drag coefficient by forcing the thickness to the minimum allowed value, but maintaining the pressure gradients within certain limits to avoid premature separation.

The maximum camber in the optimal airfoil designs varies greatly, from 1.5% for the cruise condition to 8% for the stall condition, as can be observed from Fig. 7 and Table 13. As expected, the higher the lift coefficient required at the low design AOA the more camber is necessary to achieve that lift coefficient. Except for stall and cruise, the maximum camber value occurs just behind the midchord position. In the stall condition the AOA is 6 deg, and thus the maximum camber moved forward to prevent high-pressure gradients towards the trailing edge. All other cases have almost zero AOA. In cruise, the C_l required is the lowest of all cases; thus, the low-pressure

Table 13 Values of the camber and thickness at the optimal solution

Airfoil	$(z/c)_{\max}$	$(x/c)_{(z/c)\max}$	$(t/c)_{\max}$	$(x/c)_{(t/c)\max}$	$(x/c)_{t/c=0.05}$
Initial	$04.0007E-02$	$52.0000E-02$	$10.0385E-02$	$29.5000E-02$	——
UAV stall	$07.9283E-02$	$40.5000E-02$	$05.8846E-02$	$09.5000E-02$	$30.0000E-02$
UAV takeoff run	$02.8726E-02$	$52.5000E-02$	$04.8987E-02$	$32.0000E-02$	——
UAV climb gradient	$05.6347E-02$	$57.5000E-02$	$04.8978E-02$	$33.0000E-02$	——
UAV rate of climb	$02.9597E-02$	$53.0000E-02$	$04.9460E-02$	$32.0000E-02$	——
UAV cruise	$01.5548E-02$	$40.5000E-02$	$04.8899E-02$	$32.5000E-02$	——
UAV loiter	$07.5328E-02$	$55.5000E-02$	$04.9123E-02$	$32.5000E-02$	——

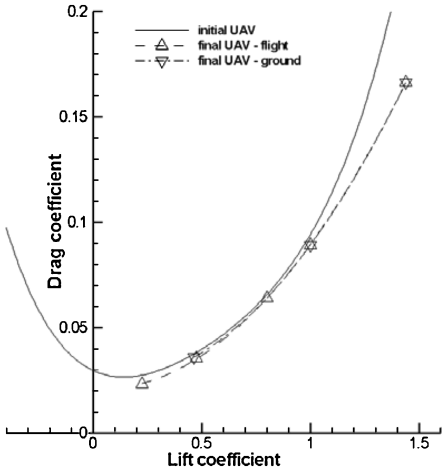

Fig. 13 Drag polars of the initial airfoil UAV and the morphing airfoil UAV.

coefficient achieved near the leading edge is sufficient to attain the required lift, and then the flow is allowed to decelerate sooner than in the other cases by reducing the camber downstream.

In all designs there was a geometric constraint forcing the thickness to be at least 1% of the chord at the control points, as mentioned earlier, except for the 20 and 40% chord position where it had a lower bound of about 5%. Figure 5 and Table 13 clearly show that the optimal airfoils are thin airfoils with the maximum relative thickness of about 5%, except for stall where it is almost 6%. The maximum thickness occurs at around 32.5% of the chord in all conditions, except for stall which occurs at 9.5%. In this case, the relative thickness reaches a value of 5% at 30% of the chord. The thicker leading edge in the stall condition is required to prevent flow separation. From Fig. 5. it can be observed that the thickness distribution is identical for all airfoils, with a slight increase at the leading edge for the stall airfoil.

B. UAV Performance Results

After having obtained an optimal airfoil for the various flight conditions, the benefits resulting from using a morphing airfoil instead of using a conventional airfoil for the complete UAV are analyzed. The drag polars of the initial and optimal airfoils are compared as well as the drag polars of the UAV with the initial and optimal airfoils. Unlike the airfoil optimization section, where the results were compared for the same AOA, the performance analysis compares the airfoil results for the same lift coefficient. Because the UAV is to be powered by a piston engine, the required installed power on both UAVs is compared to assess the truly benefits of a morphing airfoil.

The drag polar of the initial UAV, as given by Eqs. (1) and (2) and Table 2, is plotted in Fig. 13 for the various flight conditions. The drag polar of the final UAV, which uses the morphing airfoil with its different shapes at each flight condition, is also depicted in Fig. 13. The values of the drag coefficient for this curve are taken from Tables 7–12. Because it is assumed that the airfoil readily morphs to the appropriate shape at every flight condition, a continuous drag polar is obtained. The drag polars of the initial and final airfoils

Table 14 Initial and final minimum installed power for the UAV

Flight condition	P_0^{initial}, W	P_0^{final}, W	Reduction, %
Stall	2719	2083	23.4
Takeoff run	5126	5328	−3.9
Climb gradient	4475	4552	−1.7
Rate of climb	4256	4225	0.7
Cruise	3908	3326	14.9
Loiter	2133	2083	2.3

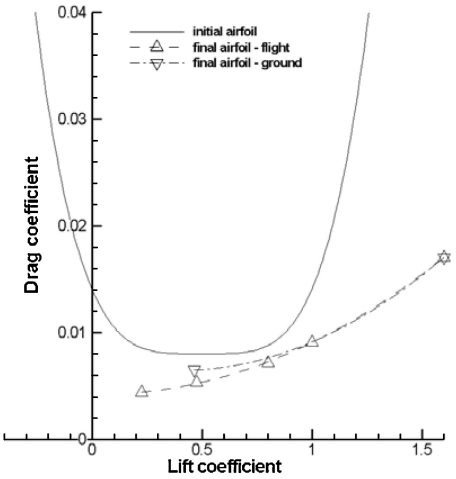

Fig. 14 Drag polars of the initial and morphing airfoils.

are shown in Fig. 14. In these figures there are two drag polars for the morphing airfoil: the flight drag polar is constructed from the in-flight conditions under which the lift balances the weight, that is, stall, climb gradient, climb rate, cruise, and loiter; the ground drag polar is constructed from the conditions on the ground, where the lift does not balance the weight, that is, takeoff run and stall.

A significant reduction in the airfoil drag coefficient is achieved with the morphing airfoil, as can be observed from Fig. 14. The reduction varies from 18.7% in the climb gradient condition to 48.9% in the cruise condition (79.6% in the stall condition). The reduction in the drag coefficient in loiter is 35.2%. Because the wing profile drag is only a fraction of the total UAV drag, the drag coefficient reduction of the complete UAV is somewhat less significant, though still important. In this case, the reduction varies from 2.5% in the climb gradient condition to 15.2% in the cruise condition (28.6% in the stall condition). The reduction in the drag coefficient in loiter is 5.3%. From these results, it is apparent that the initial airfoil was designed for the C_l range of 0.5 to 1.0, agreeing with the data of Table 2. Thus, the reduction in C_d of the optimal airfoil in this C_l range was of less significance.

Table 14 shows the minimum installed power required for each flight condition before and after the optimization of the airfoil. The propeller efficiency used in this analysis is given, in both cases, by Eqs. (5) and (6). The power setting in all conditions was assumed to be at full throttle, although in cruise one typically uses the throttle at $\frac{3}{4}$ and in loiter the power setting can be as low as half throttle. It can be observed that, despite a reduction in the drag coefficient in

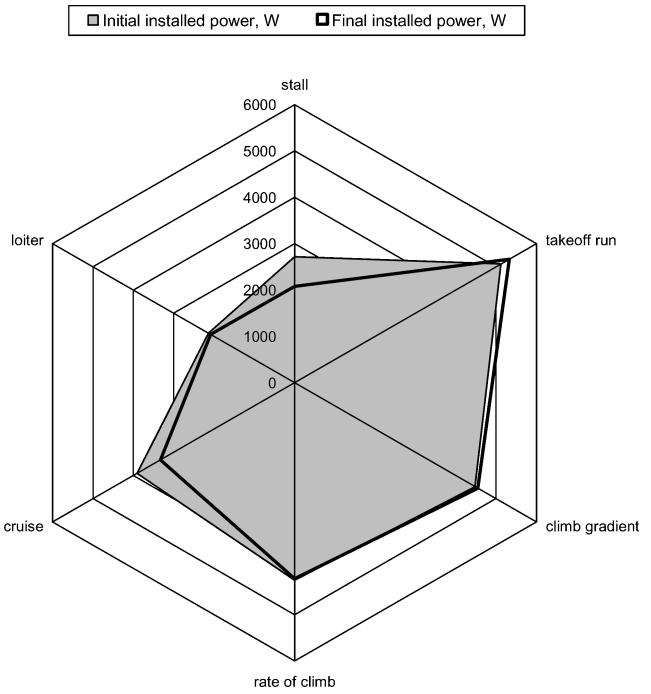

Fig. 15 Initial and final minimum installed power for the various flight conditions.

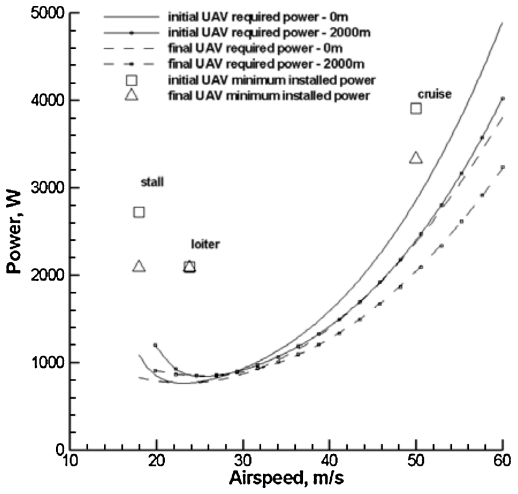

Fig. 16 Power curves for the UAV in steady level flight.

all design conditions, there is an increase in the minimum installed power in the takeoff run and climb gradient conditions. The reason for this is the nearly 2.6% increase in weight caused by the reduced airfoil thickness. As mentioned before, the great benefit from the morphing airfoil occurs at low speeds and high speeds, rather than at medium speeds. This is well illustrated in Figs. 15 and 16. This characteristic is very important because the morphing airfoil enables the UAV to perform better outside the major design point, which, in this case, is the loiter phase. By having this capability, one can either use less fuel in cruise with a reduced power setting, in which the power reduction is 15.2%, leaving extra fuel that can be used to fly farther or to stay longer over the surveillance area or even, if the same power setting is selected, the increased excess power can be used to fly a faster cruise or to accelerate faster at low speeds.

From Table 14, the minimum installed power that satisfies all flight conditions is determined by the takeoff run requirement. Based on this, and adding 500 W for the operation of the avionics, controls, and surveillance equipment, an existing gasoline engine with 5968 W (8 hp) rated power is selected. As an example of the performance gains at cruise speed and 2000-m altitude, one can observe

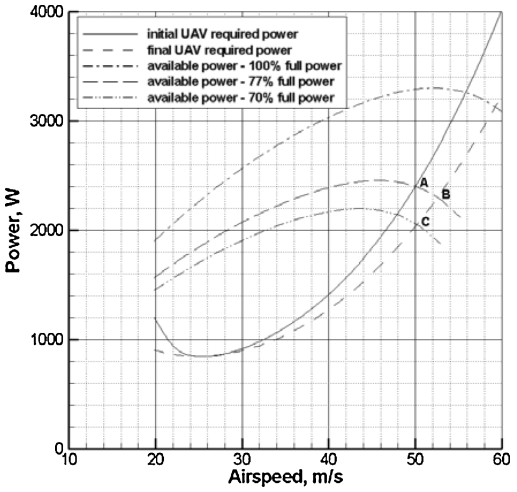

Fig. 17 Required and available power for the UAV in steady level flight at 2000-m altitude.

Fig. 17. It can be seen that the cruise for the initial UAV is flown at 77% of full power for a cruise speed of 50 m/s (point A). If the UAV is fitted with the morphing airfoil and the power setting is unchanged, there is a 5.1% increase in the cruise speed to 52.6 m/s (point B). On the other hand, if the morphing airfoil UAV flies the cruise at the same speed of 50 m/s the power setting is reduced to 70%, a 9.1% reduction (point C). In the first situation the speed increase results in a trip time reduction of 4.9%, which means 99 s less for a cruise range of 100 km. In the second case, assuming that the gasoline engine specific fuel consumption is 0.16×10^{-6} kg/Ws, the reduction in fuel used over the same distance is 0.123 kg. This is a significant reduction of 9.1%, from 1.358 to 1.235 kg, which translates to fuel costs savings in cruise of the same magnitude. If faster speeds are used for cruise, the benefits are even more important.

Although in loiter the extent of the gains are not so obvious, there are still some improvements. For example, for an unchanged loiter speed the morphing airfoil still provides a fuel reduction of 2.9%, which, for a 6-h endurance over the target, results in a reduction of 0.2 kg. The sort of fuel reductions that are obtained might seem very insignificant, but, to put it into perspective, a typical autopilot for this kind of UAV weighs less than 0.05 kg.

At low speeds greater power improvements are achieved as can be seen from Fig. 17 when comparing the full available power curve with the required power curves near the stall speed. The increased excess power enables the morphing UAV to perform maximum lift sustained maneuvers at lower speeds.

The fuel savings in the preceding example, that is, a fast cruise to a surveillance area at 100 km away from base and a loiter on site for 6 h, sums up to 0.446 kg. This value does not offset the increased weight of the UAV, which is 1.02 kg. For longer missions carried out farther away from base, a break-even point can be reached. Nonetheless, the morphing airfoil improves the overall UAV performance.

V. Conclusions

Several conclusions about the characteristics of the set of optimal airfoils for an airfoil morphing light UAV can be reached from the results from the preceding section. From Fig. 5 and Table 13, it can be observed that the optimal airfoils share a common characteristic: they all have a similar thickness distribution. The airfoil for stall, because of its high lift requirement, exhibits an increased thickness at the leading edge. The main difference between the airfoils is their camber. Although the cruise airfoil has a small camber of 1.6%, the other airfoils have a maximum camber varying up to 7.9% of the chord. Although the optimal airfoil shapes are different for each flight case, a compromise could be obtained by having only three camber line shapes: takeoff run and climb rate combined; stall, climb gradient and loiter combined; and finally cruise. By doing this, a simplified mechanism could have three predefined shapes.

It can be concluded that the morphing airfoil would be a thin airfoil and would require two morphing mechanisms. The first mechanism would be used to control the camber of the airfoil by deforming the airfoil camber line shape as necessary. The second mechanism would be used to control the thickness variations at the leading edge required for higher angles of attack, and it could be, for example, an inflatable system. On the other hand, a single morphing mechanism could be adopted if an efficient constant thickness distribution were chosen and the camber was varied at will.

Although the power reduction attained by the use of the morphing airfoil is not very high at the major design flight condition, it is significant elsewhere. Therefore, the flight envelope can be extended, and the mission profile can be more flexible in terms of flight regimes and even in sustained manoeuvrability at low speeds. No great detail was used in the analysis to accommodate the increased weight of the morphing airfoil UAV resulting from the reduced thickness of the wing and the extra systems required to perform the morphing. Furthermore, the optimization analysis was applied to the airfoil alone and not to the complete aircraft. These aspects were beyond the scope of this paper but should be addressed in future work. The real benefits of a morphing airfoil can be assessed only with a multidisciplinary design optimization tool, which takes into consideration not only the aerodynamics but also the structure and the associated systems that support the morphing. Further studies must be pursued in this area with finite wings.

Acknowledgments

This research was supported by a National Sciences and Engineering Research Council of Canada (NSERC) Discovery grant. M. Secanell acknowledges financial support from NSERC and the University of Victoria.

References

[1]Love, M., Zink, P., Stroud, R., Bye, D., and Chase, C., "Impact of Actuation Concepts on Morphing Aircraft Structures," AIAA Paper 2004-1724, April 2004.

[2]Bae, J.-S., Seigler, T., Inman, D. J., and Lee, I., "Aerodynamic and Aeroelastic Considerations of a Variable-Span Morphing Wing," AIAA Paper 2004-1726, April 2004.

[3]Ramrkahyani, D., Lesieutre, G. A., Frecker, M., and Bharti, "Aircraft Structural Morphing Using Tendom Actuated Compliant Cellular Trusses," AIAA Paper 2004-1728, April 2004.

[4]Gano, S. E., Pérez, V. M., Renaud, J. E., Batill, S. M., and Sanders, B., "Multilevel Variable Fidelity Optimization of a Morphing Unmanned Aerial Vehicle," AIAA Paper 2004-1763, April 2004.

[5]Rusell, M. T., Gano, S. E., Pérez, V. M., Renaud, J. E., and Batill, S. M., "Morphing UAV Pareto Curve Shift for Enhanced Performance," AIAA Paper 2004-1682, April 2004.

[6]Hicks, R., and Henne, P., "Wing Design by Numerical Optimization," *Journal of Aircraft*, Vol. 15, No. 7, 1978, pp. 407–412.

[7]Huyse, L., Padula, S., Lewis, R., and Li, W., "Probabilistic Approach to Free-Form Airfoil Shape Optimization Under Uncertainty," *AIAA Journal*, Vol. 40, No. 9, 2002, pp. 1764–1772.

[8]Nemec, M., and Zigg, D., "Multi-Point and Multi-Objective Aerodynamic Shape Optimization," AIAA Paper 2002-5548, Sept. 2002.

[9]Reuther, J., Alonso, J., Jameson, A., Eimlinger, M., and Saunders, D., "Constrained Multipoint Aerodynamic Shape Optimization Using an Adjoint Formulation and Parallel Computers: Part I," *Journal of Aircraft*, Vol. 36, No. 1, 1999, pp. 51–60.

[10]Reuther, J., Alonso, J., Jameson, A., Eimlinger, M., and Saunders, D., "Constrained Multipoint Aerodynamic Shape Optimization Using an Adjoint Formulation and Parallel Computers: Part II," *Journal of Aircraft*, Vol. 36, No. 1, 1999, pp. 61–74.

[11]Martins, J., "A Coupled-Adjoint Method for High-Fidelity Aero-Structural Optimization," Ph.D. Dissertation, Dept. of Aeronautics and Astronautics, Stanford Univ., Stanford, CA, Nov. 2002.

[12]Raymer, D. P., *Aircraft Design: A Conceptual Approach*, 3rd ed., AIAA Education Series, AIAA, Reston, VA, 1999.

[13]Magagnato, F., "SPARC Manual (Structured Parallel Reseach Code)," Dept. of Fluid Machinery, Univ. of Karlsruhe, Karlsruhe, Germany, 2000.

[14]Vanderplaats Research and Development, Inc., *DOT: Design Optimization Tools Users Guide*, ver. 5.0, Colorado Springs, CO, 2001.

[15]Secanell, M., and Suleman, A., "Sequential Optimization Algorithms for Aerodynamic Shape Optimization," AIAA Paper 2004-4631, 2004.

[16]Secanell, M., and Suleman, A., "Numerical Evaluation of Optimization Algorithms for Low Reynolds Number Aerodynamic Shape Optimization," *AIAA Journal*, Vol. 43, No. 10, 2005, pp. 2262–2267.

[17]Tsai, H. M., Wong, A. S. F., Cai, J., Zhu, Y., and Liu, F., "Unsteady Flow Calculations with a Parallel Multiblock Moving Mesh Algorithm," *AIAA Journal*, Vol. 39, No. 6, 2001, pp. 1021–1029.

[18]Secanell, M., "Development of a Design Tool for Aerodynamic Shape Optimization of Airfoils," M.A.Sc. Thesis, Dept. of Mechanical Engineering, Univ. of Victoria, Victoria, BC, Canada, 2004.

N. Alexandrov
Associate Editor